A Current-Driven Six-Channel Potentiostat for Rapid Performance Characterization of Microbial Electrolysis Cells

Tom R. Molderez⬤, Xu Zhang, Korneel Rabaey, and Marian Verhelst

Abstract—**Knowledge of the performance of microbial electrolysis cells under a wide range of operating conditions is crucial to achieve high production efficiencies. Characterizing this performance in an experiment, however, is challenging due to either the long measurement times of steady-state procedures or the transient errors of dynamic procedures. Moreover, wide parallelization of the measurements is not feasible due to the high measurement equipment cost per channel. Hence, to speedup this characterization and to facilitate low-cost, yet widely parallel measurements, this paper presents a novel rapid polarization curve measurement procedure with a dynamic measurement resolution that runs on a custom six-channel potentiostat with a current-driven topology. As case study, the procedure is used to rapidly assess the impact of altering pH values on a microbial electrolysis cell that produces H_2. A $\times 2$–$\times 12$ speedup could be obtained in comparison with the state-of-the-art, depending on the characterization resolution (16–128 levels). On top of this speedup, measurements can be parallelized up to $6\times$ on the presented, affordable—42\$-per-channel—potentiostat.**

Index Terms—**Analog circuits, bioelectric phenomena, closed-loop systems, electrochemical devices, iterative algorithm, measurement, microorganisms, PI-control, real-time systems, search methods.**

I. INTRODUCTION

MICROBIAL-DRIVEN chemical production is a key aspect for a circular economy [1]. Many of these various bioproduction processes are not only catalyzed by microorganisms but also driven by electricity. Communities of microorganisms partially extract the otherwise lost energy in, for example, wastewater treatment in a bio-electrochemical system (BES) [2]. Originally, the research community developed BESs that directly generate electrical power from the consumed organic waste streams, "microbial fuel cells." More recently, the research focus has shifted to "microbial electrolysis cells" (MECs) to which electrical power is added to enable reactions otherwise thermodynamically not feasible. The most simple outcome of such an MEC is the production of H_2 from wastewater at high-efficiency and low-power input [3].

Whereas considerable research has focused on improving the maximal MEC volumetric production performance under optimal, laboratory conditions [4], [5], less attention has gone toward a measurement instrument to study the impact of out-of-the-lab operating conditions on the MEC performance. From an application perspective, the MEC operating environment generally consists of two categories: 1) external conditions such as pH, the influent composition, or the temperature which are difficult to control [6], [7] and 2) configurable settings, such as the electrical settings. The relation between these electrical settings and the production performance, obtained from a polarization curve measurement for a particular MEC for realistic, possible suboptimal external conditions, allows to nevertheless maintain a high production performance.

An MEC is a dynamic system with a slow transient response to external stimuli, an evolution over time, and an inherent variation between similar samples [4]. Therefore, characterizing the impact of external conditions on the MEC polarization curve with a predefined measurement with static measurement resolution is either slow [e.g., chronoamperometry (CA)] or contains transient measurement errors [e.g., cyclic voltammetry (CV)] [8]–[10].

Commercial potentiostats [11], [12] with multiple channels are expensive, limiting the practical deployment of multiple channels. Low-cost potentiostats [13]–[15] only contain a single channel with an analog potential loop using an operational amplifier in negative feedback. This feedback loop is not capable of driving the large capacitive load of electroactive biofilms. State-of-the-art potentiostats [16]–[18] are not suitable for the large capacitive load because they also use a similar operational amplifier (opamp) in negative feedback. The state-of-the-art multichannel instruments either lack the current driving [19], [20] or drive each channel sequentially instead of continuously [21]–[23].

In addition, none of the existing potentiostat measurement instruments is able to dynamically alter their measurement resolution to speedup the characterization measurement time.

To reduce this characterization measurement time, this paper introduces the following two novelties: 1) an affordable multichannel potentiostat suitable for microbial electrochemical electrodes and 2) a rapid polarization curve measurement procedure using a dynamic measurement resolution. As case study, the impact of pH on the polarization curve of an MEC producing H_2 is assessed using both novelties.

This article has been accepted for inclusion in a future issue of this journal. Content is final as presented, with the exception of pagination.

2   IEEE TRANSACTIONS ON INSTRUMENTATION AND MEASUREMENT
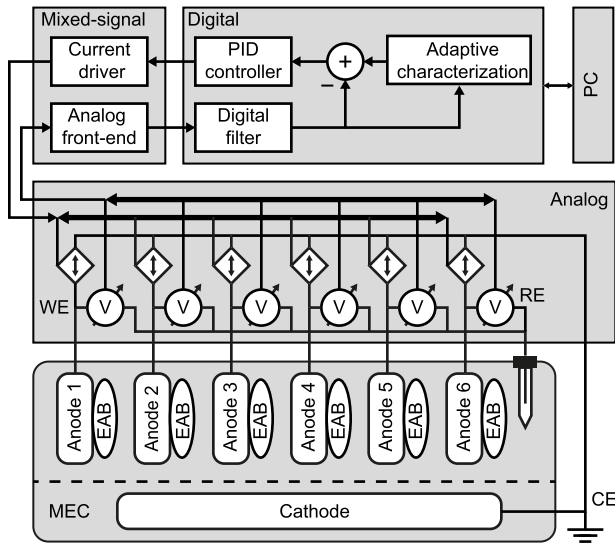

Fig. 1.   Overview of the measurement setup.

This paper is organized as follows. First, the six-channel potentiostat and the rapid polarization curve measurement procedure are discussed in Section II. Next, Section III discusses the system implementation. Section IV compares our procedure with the state-of-the-art for assessing the impact of pH on an MEC. Finally, Section V concludes this paper.

II. PROPOSED MEC PERFORMANCE CHARACTERIZATION

To study the impact of external conditions, such as the pH, on the polarization curve of a microbial electrochemical electrode, the state-of-the-art uses a standard three-electrode measurement setup controlled by a potentiostat [24]. To characterize the MEC's behavior in function of pH, this setup measures the electrode current at different potentials for each pH setting of interest. Each single measurement, however, is time intensive due to the MEC's slow dynamic behavior. Furthermore, these measurements must be multireplicated to achieve statistic relevant results.

Our proposed, alternative measurement approach is shown in Fig. 1. This setup consists of an MEC with six individual biotic electrodes as working electrodes in a common two-chamber bioreactor with a counter electrode and a reference electrode. The analog circuitry delivers current to each electrode and measures the corresponding potential, the voltage difference between the WE and the RE. The mixed-signal unit converts the signals between the analog domain and the digital domain. Next, the digital unit controls the potential with a PID controller. Finally, a novel rapid polarization curve measurement procedure determines the potential points to measure. Section II-A will first explain the six-channel potentiostat, and Section II-B will explain the rapid polarization curve measurement procedure.

A. Affordable Six-Channel Potentiostat

The state-of-the-art custom-made potentiostat systems supporting a three-electrode setup use an analog potential control loop [13]–[18], [21]–[23]. The opamp in negative feedback maintains the potential equal to the setpoint [Fig. 2(a)]. While
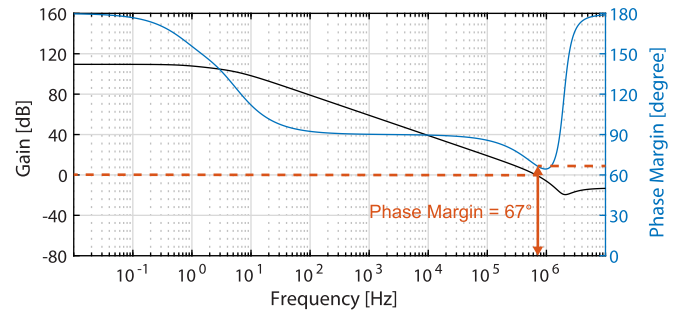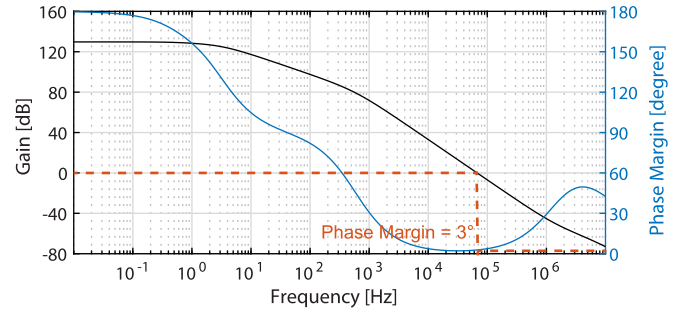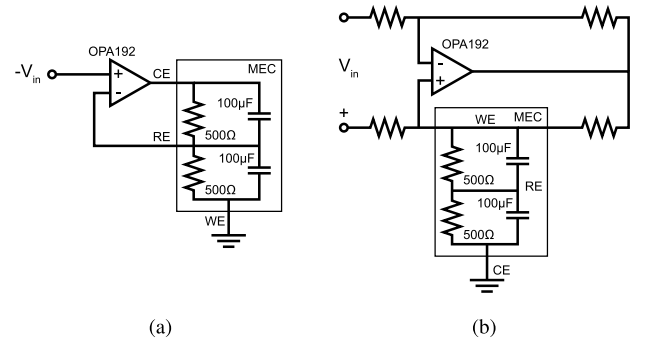

Fig. 2.   Stability analysis of a potentiostat with an MEC capacitive load for an opamp architecture, with (a) circuit and (c) simulated open-loop phase margin, respectively, for a current pump architecture, with (b) circuit and (d) simulated open-loop phase margin.

this loop results in a low-cost system, the phase margin of the analog potential loop quickly deteriorates for capacitive loads [25], which are typical for MECs, resulting in unstable behavior, as shown in Fig 2(c), simulating the open-loop transfer function.

Straightforward compensation techniques are either not possible, such as gain compensation or out-of-loop compensation, due to the circuit architecture, or reduce the stability even more, such as lead compensation or in-loop compensation. More complex compensation techniques that shift the load pole to higher frequencies or that introduce an additional zero require either the load to be known or a trial-and-error procedure [26]–[30]. The biotic electrode impedance load is unknown and varies between operating potentials, between samples, and over time, rendering this procedure unsuitable for our measurement setup. Trial-and-error procedures will inevitably introduce voltage spikes which generate oxygen in the setup and thereby kill the anaerobic microorganisms.

This article has been accepted for inclusion in a future issue of this journal. Content is final as presented, with the exception of pagination.

MOLDEREZ *et al.*: CURRENT-DRIVEN SIX-CHANNEL POTENTIOSTAT

3

Therefore, we have opted, as a first, to switch from a voltage- to a current-driven architecture using a Howland current pump topology [Fig. 2(b)]. The feed-forward path sources or sinks a digital controlled current, while the feedback path measures the WE potential. A digital controller then determines the amount of driving current to maintain the potential equal to the target potential, set by the rapid polarization curve measurement procedure.

The major advantage of this architecture is that it remains stable for large capacitive loads, illustrated in Fig. 2(d), simulating the open-loop transfer function. As a result, no additional compensation is required. The downside of this topology, that it delivers only a limited amount of maximum current, in the order of milli ampere, is not a drawback for our characterization, but explains why this circuit is not used in high-current electrochemical testing [31].

The control of the potential then occurs in the digital domain with a configurable PID controller. Based on the difference between the measured potential and the target potential, the PID-controller determines the stimulation current.

B. Rapid Polarization Curve Measurement Procedure

The MEC continuous longtime current production is expressed by the polarization curve [5]. This curve indicates which overpotential E is required for a particular current I and corresponding reaction rate Q in a particular environment. Each measurement point of this curve is only valid for the MEC being in steady state, thus lasting for at least $T > 3 \dots 5\tau$, where τ is the dominant MEC time constant. Therefore, investigating the impact of the environment on the MEC polarization curve and correspondingly longtime MEC operation is time intense.

As its second contribution, this paper introduces a novel rapid polarization curve measurement that does not result in a hysteresis, such as a CV and, for equal precision, is much faster than a staircase CA. Instead of using preconfigured, equidistant potential measurement points with step E_r [Fig. 3(a)], our procedure determines at runtime which potential points to measure in a data-driven way. The measurement procedure uses a performance metric J for this, to evaluate how relevant a measurement point is, together with a nonlinear search procedure to quickly measure the polarization curve nonequidistantly, i.e., E_{r1} versus E_{r2} [Fig. 3(b)]. As such, a high accuracy is achieved in the region of interest.

To determine this region of interest, two different performance metrics were used as case study in this paper. The first metric, J_{H_2}, expresses the net MEC power generation (in H_2) assuming an ideal CE [32]

$$J_{H_2}(E) = \Delta H_{H_2} Q_{H_2} - I(E) * (E_{WE} - E_{CE}) \qquad (1)$$

where ΔH_{H_2} is the H_2 enthalpy and $Q_{H_2} = I(V, e)/zF$ is the (ideal) H_2 production over time, with z the valence number of ions and F the Faraday constant. The second metric expresses the generated MEC economic value based on the difference between the H_2 cost and the electricity cost

$$J_\$(E) = p_{H_2} Q_{H_2} - p_{kWh} I(E) * (E_{WE} - E_{CE}) \qquad (2)$$

where p_{H_2} is the economic value of H_2 and p_{kWh} the economic cost of the consumed electrical power.
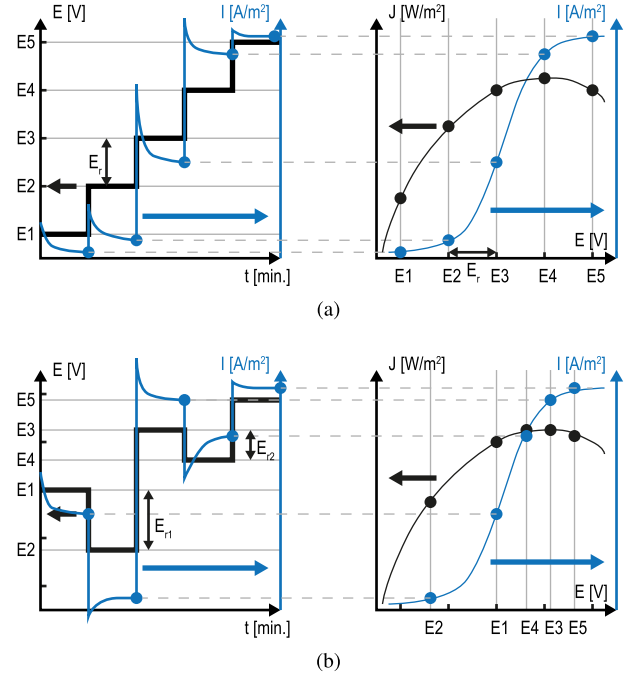

Fig. 3. Measurement of the polarization curve using (a) staircase CA resulting in equidistant potential measurement points and (b) fast polarization curve measurement with nonequidistant measurement points.

To characterize the MEC polarization curve quickly yet precise, an algorithm is required that starts from a broad measurement interval and efficiently narrows down the sampling range to the region of interest, i.e., the region where the performance metric is the largest. The used search algorithm is an improvement from [33]. Every iteration of this algorithm contains two steps. In the first step, the next potential to be measured is derived. In the second step, the search interval is reduced based on the measurement done in the first step. The algorithm converges quickly around the region where the performance metric is the largest, resulting in a focus of the characterization accuracy around the region of interest.

Algorithm 1 Robust Nonuniform Search

1: **par** $r, J_{th}, [E_l, E_r]$ {resolution, threshold, characterization interval}
2: **set** $S(E, J)$ {ordered set in E}
3: $S \leftarrow [(E_l, -\inf), (E_r, -\inf)]$
4: **while** $E_r - E_l > r$ **do**
5:     **var** $E_k \leftarrow \max(\min(d(E_k, E_i \in S[E_l : E_r])))$ {if 2 or more, take the one closest to $\text{mean}(E_l, E_r)$}
6:     $S.\text{add}(E_k, J_k)$ {iteration k}
7:     **for all** (E_i, J_i) in $S[E_l : E_r]$ **do**
8:         $[J_m, E_m] = \max(S(J))$
9:         $E_l \leftarrow E_i$ **if** $E_i < E_m$ && $J_i < J_m - J_{th}$
10:        $E_r \leftarrow E_i$ **if** $E_i > E_m$ && $J_i < J_m - J_{th}$
11:    **end for**
12: **end while**

The pseudocode of the complete polarization curve characterization algorithm is given in Algorithm. 1. In this algorithm $[E_l, E_r]$ is the initial potential range and r is the
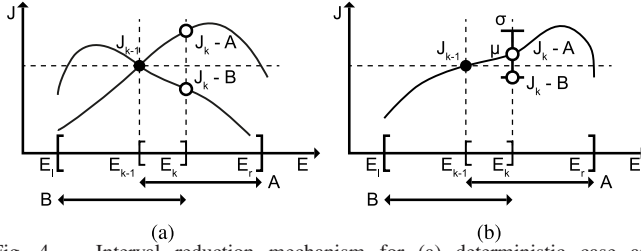
This article has been accepted for inclusion in a future issue of this journal. Content is final as presented, with the exception of pagination.

4   IEEE TRANSACTIONS ON INSTRUMENTATION AND MEASUREMENT

Fig. 4.   Interval reduction mechanism for (a) deterministic case and (b) stochastic case.

Fig. 5.   Current feed-forward path circuitry.

Fig. 6.   DC accuracy for the different channels of the current feed-forward circuitry.

minimum measurement resolution. This algorithm contains two improvements in comparison to [33]. In the first step, the original algorithm determined the next characterization point based on the maximum of a fitted parabola through the previous three measurement values. This results in an unpredictable and uncontrollable distribution of measurement samples. In the current work, the next measurement point was taken instead as the potential within the search range that is farthest separated from all previous measured potentials (Algorithm 1, lines 5 and 6). In the second step, the original algorithm assumed that there was no noise disturbance on the measurement samples. Fig. 4(a) illustrates the interval reduction mechanism for measurement samples without noise. If a new measurement value (J_k) is larger than that of the previous value (J_{k-1}), as in case A, the location of the maximum is limited to subinterval A because of unimodality. Similarly, if a new measurement value is smaller than that of the previous value, as in case B, the location of the maximum is limited to subinterval B. Noise on the measurement point might flip the relative orientation of J_k and J_{k-1} which could result in an error. For example, in Fig. 4(b), due to noise, the search interval might incorrectly be narrowed to interval B instead of to interval A. By assuming Gaussian noise, $J_k \sim N(\mu_k, \sigma_k)$, in worst-case, the samples would have an equal mean resulting in a flipping error probability of $P_e = P(J_{k-1} - J_k > 0) = 50\%$. Therefore, this paper introduces a configurable threshold J_{th} in the interval reduction mechanism. Measurement samples are only considered to have a different value, if $|J_i - J_j| > J_{th}$ (Algorithm 1, lines 7–11). Thus, in comparison with [33], the probability of a flipping error in worst-case scenario is strongly reduced because of this noise masking, equalling: $P_e = P(J_{k-1} - J_k > J_{th})$. Configuring $J_{th} \gg \sigma_k$, however, reduces the obtained accurarcy in J^* as more and more samples are treated equally.

A closed expression of the worst-case convergence rate requires an additional constraint: J fulfills $(J(E^*) \pm J_{th}) > (\forall E \neq E^* : J(E) \pm J_{th})$. If three or more samples are indistinguishable, then they are guaranteed to lie within J_{th} of $J(E^*)$ and Algorithm 1 has converged. The interval length $N(k)$ for iteration k and corresponding worst-case convergence rate $k(r)$ then equal

$$N(k) = N/2^{(k-1)/2}, \quad k = 1, 3, 5, \ldots \tag{3}$$
$$k(r) \leq 2 * \log_2(N/r) + 1 \tag{4}$$

where $N = E_r - E_l$ is the original characterization interval length. As a result, in comparison with [33], worst-case convergence remains superlinear.
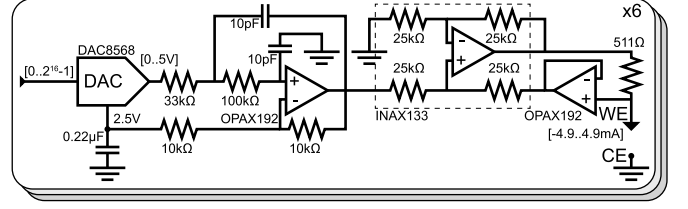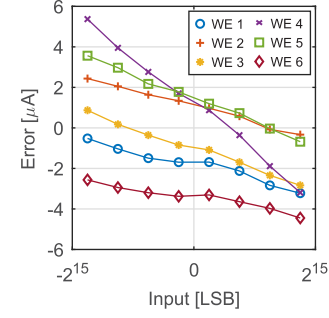
III. SYSTEM IMPLEMENTATION

The six-channel potentiostat consists of analog- and mixed-signal hardware, implemented with PCB technology and off-the-shelf components, and digital hardware, implemented with a commercial microcontroller executing the control software [Fig. 1]. The total platform cost equaled 250 \$. The total power consumption at maximum output current of each channel was 2.3 W.

A. Analog Hardware

The two functions of the analog hardware are: 1) to deliver current to each of the six electrodes and 2) to measure the corresponding potential of each of the six electrodes. The common CE is connected to the electronic ground.

Fig. 5 shows the six times repeated current driver with bipolar current pump. A common eight channel, 16b, DAC (DAC8586, TI), with six channels enabled and two channels disabled, is used to convert the digital control signals into analog control signals. The output signal of each DAC channel is converted to a bipolar voltage signal using an active, second-order Bessel filter, which minimizes overshoot. This filter is implemented with a Sallen–Key topology. The voltage-controlled current pump is implemented with a modified Howland current source architecture [34]. The modified architecture requires a single resistor to set the transconductance gain instead of a matched pair. However, an additional amplifier is required in the negative feedback path of the current pump. A special-purpose difference amplifier with integrated, trimmed resistors (INA2133, TI) is used for implementation of the current pump.

The additional amplifier of the modified Howland current pump has no impact on the stability of the feedback loop due to its ideal behavior in the frequency region of interest. The phase margin remains at 67°.
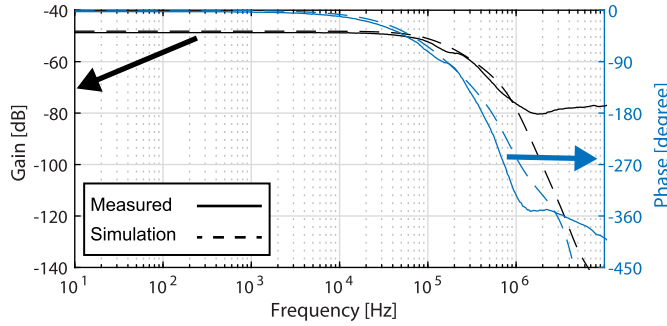
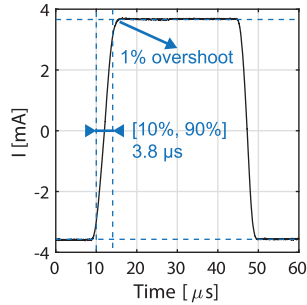Fig. 7. Transfer function of the drive channel.

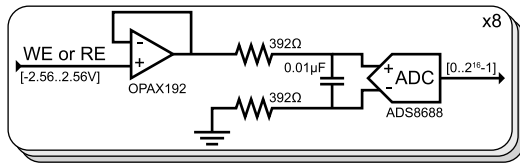Fig. 8. Step response of the drive channel.

Fig. 9. Potential measurement feedback circuitry.

The digital-to-current dc transfer function equals:

$$H_I(I_b) = 5 \text{ V}/511 \ \Omega * (I_b - 2^{15})/2^{16} \qquad (5)$$

where $I_b = [0, 2^{16} - 1]$. The current output has a range of $[-4.9 \text{ mA}, 4.9 \text{ mA}]$ with a resolution of 150 nA. Fig. 6 shows the static dc current error of each channel. The maximum error is about 6 μA resulting in a relative precision of at least 0.12%.

Fig. 7 compares the simulated AC transfer function with the measured AC transfer function. The dominant pole occurs at 50 kHz to allow signal frequencies up to 5 kHz without distortion. The measured step response for a 50% step is shown in Fig. 8. The rise time is below 4 μs with an overshoot of only 1%.

The potential of each WE is measured by measuring both the voltage of this electrode and the voltage of the common RE. The potential is then obtained by taking the difference of both voltages by the microprocessor. Fig. 9 shows the circuit topology of one of the eight voltage measurement units (six for the WE and two for the RE). First, the voltage is buffered using a low-offset opamp (OPAX192, TI). Next, a passive pseudodifferential low pass filter with a pole at 20 kHz is used to prevent aliasing. An eight-channel, 16b, bipolar input, successive approximation ADC (ADS8688, TI) is used to digitize the signals. Because this ADC directly

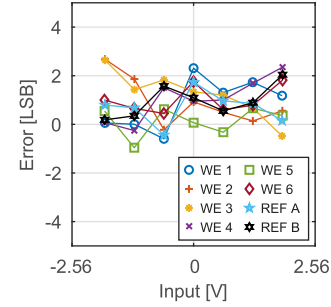Fig. 10. DC accuracy for the different channels of the feedback voltage measurement circuitry.
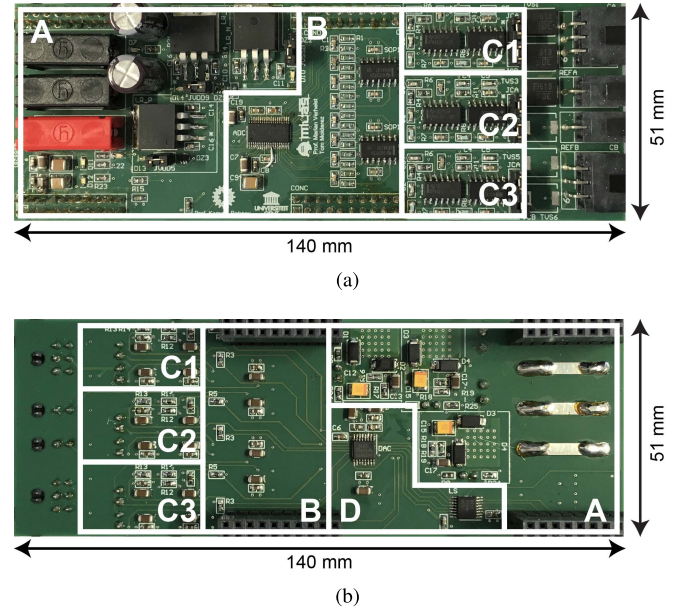

(a)

(b)

Fig. 11. Analog PCB with A—power supply, B—eight-channel voltage measurement, C—3× two-channel current pump, and D—eight-channel DAC [35]. (a) Front view. (b) Back view.

supports bipolar input signals, the cost and components of the input stage are greatly reduced. The sample rate of each channel is 25 kHz.

The voltage-to-digital dc transfer function equals

$$H_V(V) = (V + 2.56 \text{ V})/5.12 \text{ V} * 2^{16} \qquad (6)$$

where $V = [-2.56 \text{ V}, 2.56 \text{ V}]$, the measurement range. The measurement resolution is 78.125 μV. Fig. 10 shows the static dc measurement error of each channel. The maximum error is three LSB resulting in an actual precision of at least 0.01%.

Fig. 11 shows the PCB. The front side contains the power supply, the ADC, and the current pumps (3× two channels). The back side contains the DAC and auxiliary components. The PCB layer stack contains four layers: the top signal layer, an internal ground plane, an internal power plane, and a bottom signal layer. The total board area is 71.4 cm^2.

B. Control Software

The control software runs on a C2000 Delfino microcontroller (TMS320F28377S, TI), a high-performance microcontroller suitable for digital feedback applications. Appririate alternative microcontrollers are those with $\approx$200 MOPS

computational power, such as the PIC or SAM family of Microchip or the STM32 family of STMicroelectronics. Each of the eight channels (six WE channels and two RE channels) could run an individual control algorithm. The controllers of all eight channels are scheduled in round robin at 25 kHz.

A single hardware timer throws an interrupt every 5 μs to trigger the execution of the next channel's control algorithm. In case this channel is a WE, the following steps are executed. First, the WE voltage of the channel is measured and the potential is calculated from this measured voltage and the voltage of the RE electrode. Next, the PID controller determines the output current from the difference between the measured potential and the target potential, set by the fast polarization measurement algorithm. Finally, if the measurement time surpasses T, the new target potential is calculated, using Algorithm 1. In case this channel is an RE channel, only the RE voltage is measured. This voltage is then used by the WE channels to calculate their potential.

The response time of the complete end-to-end (measurement-to-stimulation) control loop is <9 μs (2 μs because of the ADC sampling, <5 μs because of the digital PID computation, and 2 μs because of the DAC settling time). This makes the system capable of characterization of slow to medium (msec) response time systems.

IV. CASE STUDY: CHARACTERIZATION OF THE pH IMPACT ON AN MEC

The rapid polarization curve measurement procedure that runs on the six-channel potentiostat was used to characterize the pH impact on an MEC. The MEC is described first in Section IV-A. Second, the tuning of the digital PI-controller is discussed in Section IV-B. Then, the operation and convergence of the search algorithm are illustrated in Section IV-C. The results of the pH impact study on the MEC for both J_{H_2} and $J_\$$ are discussed in Section IV-D. Finally, Section IV-E compares this paper with the state-of-the-art.

A. H_2 Producing MEC

The H_2 producing MEC used in this experiment is a circular, two-chamber, bioreactor operating in a (dark) 28 °C temperature controlled room [36]. The anode compartment had a volume of 700 mL, filled with anaerobic modified M9 medium and 25 mM sodium acetate as electron donor, mixed with a magnetic stirrer at 300 r/min. Growth of the EABs occurred on six individual glassy carbon plates (25 mm × 20 mm × 2 mm). Each electrode was successively polished on microcloth pads with 1, 0.3, and 0.05 μm alumina slurries (Buehler, USA). The cathode compartment contained a cylindrical stainless steel mesh counter electrode (8 cm height and 2 cm diameter) (Solana, Belgium). The two compartments were separated by a cationic exchange membrane (Ultrex CMI-7000, 12.5 cm^2). An Ag/AgCl (3 M KCl) reference electrode (ALS, Japan, 0.205 V versus standard hydrogen electrode at 28 °C) was used to perform all the electrochemical measurements. The full grown of the EABs occurred at a fixed WE potential of −0.1 V, controlled by a CHI 1000C Multipotentiostat (CH Instruments, USA).
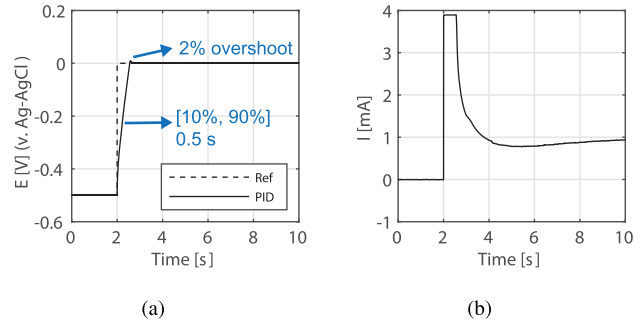

Fig. 12. Step response of a single channel of the digital potential controller on an MEC with (a) MEC potential and (b) MEC current.

Electrochemical CV experiments were done as a bench-marking reference for [−0.8 V, 0.2 V] versus Ag–AgCl with a scan rate of 5 mV s^{-1} and repeated three times, using the same CHI 1000C Multipotentiostat.

The pH of the MEC medium was measured with a Consort C532 (Consort, Belgium).

B. MEC Potential Control

The stability of the digital potential control loop for each channel is assessed with a step response of $E = 500$ mV. Fig. 12(a) shows the response of a single, representative channel. The PID-controller parameters were tuned to minimize overshoot (only 2%) because high voltage spikes could activate unwanted redox-reactions. The minimal rise time is limited by the maximum drive current (set at 80% in software) of the analog circuitry [Fig. 12(b)].

C. Logarithmic Convergence of the Search Algorithm

This section assesses the convergence rate of the search algorithm for the MEC described above. The settings of the algorithm were set as follows. The characterization interval equaled $[E_l, E_r] = [-0.8 \text{ V}, 0.2 \text{ V}]$ versus Ag–AgCl, which is the common potential range of interest for this type of MEC. The minimal resolution r was varied to illustrate the effect on the MEC convergence rate and the MEC characterization accuracy. The algorithm ran four times, with r subsequently set at 1/16 V(6.3%), 1/32 V(3.1%), 1/64 V(1.6%), and 1/128 V(0.8%). The threshold J_{th} was set at 1% of the (estimated) maximum of J_{H_2} and $J_\$$, respectively, and the sample period was set at $T = 3$ min (from a measured $\tau \approx 30$ s). Before and after all these experiments, a CV experiment was executed.

The measured samples are indicated with specific markers for each resolution experiment [Fig. 13]. Initially, for the first few iterations, the algorithm roughly characterized the MEC performance. Then, when the algorithm approached the region near maximal performance, the characterization resolution became more precise. The convergence time increased for a higher minimum resolution [from 6 iterations (18 min) for $r = 1/16$ V to 10 iterations (30 min) for $r = 1/128$ V] with a slightly better approximation of the maximal performance, as given by (3). There was an offset in measured J_{H_2} between the different experiments due to the biofilm evolution over time, which was confirmed by a change in the pre-CV experiment compared with the post-CV experiment.

This article has been accepted for inclusion in a future issue of this journal. Content is final as presented, with the exception of pagination.

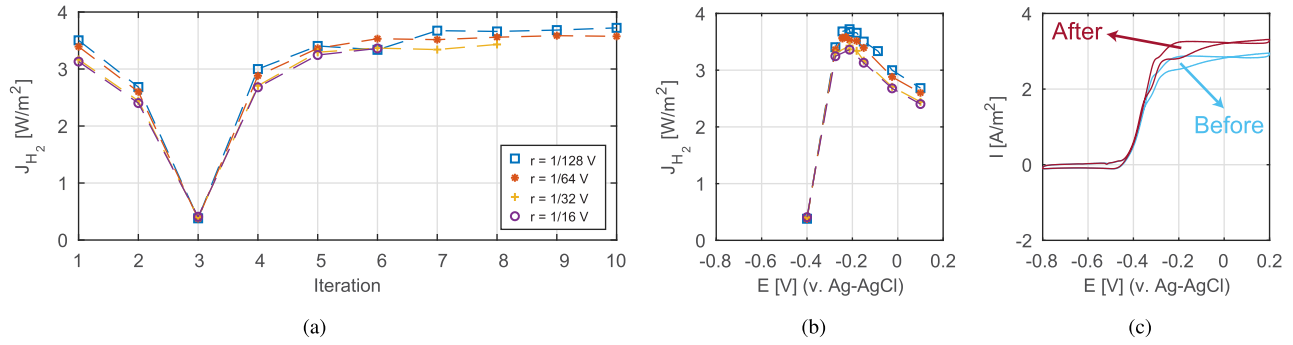MOLDEREZ et al.: CURRENT-DRIVEN SIX-CHANNEL POTENTIOSTAT

7

Fig. 13. Convergence of the robust nonuniform search algorithm for J_{H_2} with (a) subsequent iteration steps, (b) polarization curve, and (c) CV experiment before and after the four search experiments.

The nonuniform nature of the search algorithm results in a nonequidistant spread of the measured samples. As can be seen in Fig. 13(b), the complete characterization interval is sampled, yet there are more measurements in the region of interest, i.e., the region near maximal performance, than at the border of the characterization interval. A linear search algorithm with equal accuracy would take, for $r = 1/16$ V, 16 iterations (48 min) to, for $r = 1/128$ V, 128 iterations (384 min). Our proposed fast characterization procedure thus achieves a $2\times-12\times$ speedup with equal resolution in the region of interest. Finally, measurements were taken at steady-state without the transient errors typical for a CV measurement.

D. pH Impact on an MEC

In the last experiment, the impact of the pH on each of the six bio-electrodes of the MEC was characterized simultaneously. The rapid polarization curve measurement procedure ran in parallel with three channels configured for J_{H_2} and three channels configured for $J_\$$. Each run was repeated twice. In $J_\$$, p_{H_2} was taken as 2\$/kg [37] and p_{kWh} was taken as 0.16\$/kWh, the New York 2007 commercial electricity cost. A CV measurement was done for each channel as control. The pH of the cultured medium was subsequently set at 7, 6, 5, 7.5, 8, and 9. For each pH setpoint, we first report the performance of one J_{H_2} and one $J_\$$ channel. Later we show within experiment variations across all three J_{H_2} and $J_\$$ channels. For a pH of 9, no measurement data is given because the current dropped below the minimum measurement resolution.

Fig. 14(a) and (b) show the CV curve and the J_{H_2} curve of a single biotic MEC anode. The CV graph shows that the pH had a major impact on the maximal current. The J_{H_2} graph shows a similar trend for the maximal performance. On top of that, because no hysteresis was present in comparison with the CV measurement, this difference was quantized in a relevant metric, from 0.1 W/m^2 at pH of 5 to 3.6 W/m^2 at pH of 7.5. The same observation held for the $J_\$$ performance metric. The pH had a major impact on the maximal current [Fig. 14(c)] and the maximal performance [Fig. 14(d)].

The measurement data of both performance metrics for the $2\times$ repeated three-channel parallelized experiments were statistically processed. The mean and standard deviation of the optimal potential and current maximizing J_{H_2} and $J_\$$, respectively, are shown in Fig. 15(a). For both metrics, the potential for which optimal performance was reached, shifted with about
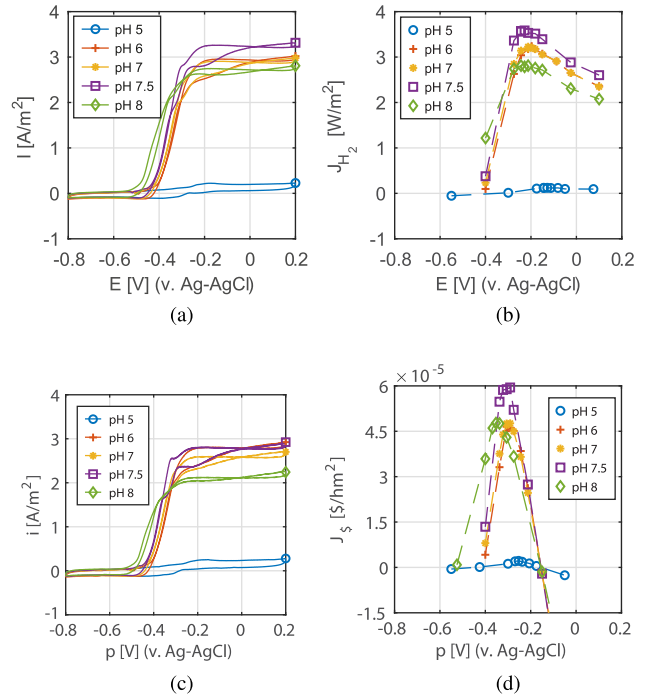
Fig. 14. Influence of pH on J_{H_2} with (a) CV measurement and (b) fast characterization procedure. Influence of pH on $J_\$$ with (c) CV measurement and (d) fast characterization procedure.

Fig. 15. Influence of pH for $J_{H_2} \pm \sigma$ and $J_\$ \pm \sigma$ on (a) optimal potential and the optimal current and (b) maximal performance.

100 mV due to the pH shift. The mean and standard deviation of the maximal performance are shown in Fig. 15(b). For both cases, maximal performance was achieved at pH of 7.5 and was 14% higher for J_{H_2} and 26% higher for $J_\$$ than at neutral pH. These results agree with [38], [39] and moreover quantify them.
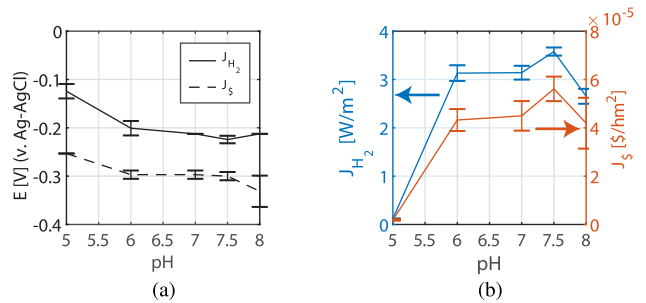
TABLE I

SPECIFICATIONS OF TYPICAL COMMERCIAL INSTRUMENTS, THE STATE-OF-THE-ART AND THIS PAPER

Instrument	PalmSens [11]	Biologic [12]	2011 [13]	2012 [14]	2012 [21]	2015 [22]	2016 [23]	**This work**
Potential range	$\pm 4\,V$	$\pm 10\,V$	-	$\pm 990\,mV$	$\pm 2\,V$	$0\,V \ldots 2.5\,V$	$0\,V \ldots 3.3\,V$	$\mathbf{\pm 2.56\,V}$
Potential resolution	$125\,\mu V$	$5\,\mu V$	-	-	$3\,\mu V$	$38\,\mu V$	$3.2\,mV$	$\mathbf{78\,\mu V}$
Current range	$\pm 100\,mA$	$\pm 400\,mA$	$\pm 2\,mA$	$\pm 10\,\mu A$	$\pm 10\,\mu A$	$\pm 25\,\mu A$	$\pm 103\,\mu A$	$\mathbf{\pm 4.9\,mA}$
Current resolution	$1\,pA$	$760\,pA$	$200\,nA$	$100\,nA$	$5\,pA$	$760\,pA$	$50\,pA$	$\mathbf{150\,nA}$
Signal frequency	$500\,Hz$	$1\,MHz$	-	$1\,kHz$	$100\,kHz$	-	-	$\mathbf{5\,kHz}$
WE channels	12	5	1	1	1	1	1	**6**
Cost-per-channel	1k \$	10k \$	600 \$	110 \$	-	-	-	$\mathbf{< 42\$}$
Bioanode stable	Yes	Yes	No	No	No	No	No	**Yes**
Measurements	Static	Static	Static	Static	Static	Static	Static	**Dynamic**

E. Comparison With the State-of-the-Art

The specifications of the six-channel potentiostat are compared with commercial potentiostats [11], [12], low-cost potentiostats [13], [14], and state-of-the-art multichannel potentiostats [21]–[23] (Table I).

In comparison with commercial potentiostats, the six-channel potentiostat achieves a similar relative current and voltage precision (0.1%), although at a reduced range, optimized for MECs. As a result, a more cost-effective analog electronic design could be used to achieve a $\times 20$–$\times 200$ cost reduction. Furthermore, the six-channel potentiostat measures the polarization curve with a dynamic resolution compared to the static measurement techniques of commercial devices, where measurement points are predefined, resulting in a $2\times$–$12\times$ measurement speedup for typical measurement accuracies.

In comparison with low-cost alternatives, our devices contains six individual channels, with a $5\times$ higher maximum signal frequency and a $2.5\times$–$14\times$ lower cost. Moreover, the six-channel potentiostat is stable for bioanode loads and supports a dynamic measurement resolution.

In comparison with state-of-the-art multichannel potentiostats [21]–[23] that drive each channel with the same potential, each of our six potentiostat channels is controllable with an individual potential to allow truly parallel experiments.

While both the commercial devices and the lowcost alternatives do not dynamically alter the measurement resolution, it is possible to add the rapid polarization curve measurement procedure to the control firmware.

V. CONCLUSION

This paper presented a novel, rapid polarization curve measurement procedure together with a low-cost six-channel potentiostat to quickly assess the impact of external disturbances on an MEC. By defining a performance tradeoff metric, the robust nonuniform search procedure measures the MEC performance with high resolution only in the region of interest. As a result, the measurement time is logarithmic dependent on the measurement resolution instead of linear. A practical speedup of $2\times$–$12\times$ in comparison with a CA sweep was achieved when assessing the pH on an MEC case study. In addition, no transient measurement errors occurred in comparison with a CV measurement.

The newly developed potentiostat overcomes the inability of commercial potentiostats to execute this real-time iterative algorithm. Moreover, custom-made potentiostats might become unstable due to the large capacitive load of the bioanode. Therefore, the potentiostat contained a current-driven architecture with a digital potential control loop. This digital feedback loop is tunable to achieve the targeted dynamic response. Finally, the six channels with an affordable 42 \$-per-channel cost allow to duplicate experiments for statistic relevant results and further speedup multicell characterization.

REFERENCES

[1] H. D. Beyene, A. A. Werkneh, and T. G. Ambaye, "Current updates on waste to energy (WtE) technologies: A review," *Renew. Energy Focus*, vol. 24, pp. 1–11, Mar. 2018.

[2] B. E. Logan and K. Rabaey, "Conversion of wastes into bioelectricity and chemicals by using microbial electrochemical technologies," *Science*, vol. 337, no. 6095, pp. 686–690, Aug. 2012.

[3] B. E. Logan et al., "Microbial electrolysis cells for high yield hydrogen gas production from organic matter," *Environ. Sci. Technol.*, vol. 42, no. 23, pp. 8630–8640, Oct. 2008.

[4] A. Kadier, Y. Simayi, P. Abdeshahian, N. F. Azman, K. Chandrasekhar, and M. S. Kalil, "A comprehensive review of microbial electrolysis cells (MEC) reactor designs and configurations for sustainable hydrogen gas production," *Alexandria Eng. J.*, vol. 55, no. 1, pp. 427–443, Mar. 2016.

[5] B. E. Logan et al., "Microbial fuel cells: Methodology and technology," *Environ. Sci. Technol.*, vol. 40, no. 17, pp. 5181–5192, Jul. 2006.

[6] E. S. Heidrich, S. R. Edwards, J. Dolfing, S. E. Cotterill, and T. P. Curtis, "Performance of a pilot scale microbial electrolysis cell fed on domestic wastewater at ambient temperatures for a 12 month period," *Bioresource Technol.*, vol. 173, pp. 87–95, Dec. 2014.

[7] A. Escapa, R. Mateos, E. Martínez, and J. Blanes, "Microbial electrolysis cells: An emerging technology for wastewater treatment and energy recovery. From laboratory to pilot plant and beyond," *Renew. Sustain. Energy Rev.*, vol. 55, pp. 942–956, Mar. 2016.

[8] E. Martin, O. Savadogo, S. R. Guiot, and B. Tartakovsky, "Electrochemical characterization of anodic biofilm development in a microbial fuel cell," *J. Appl. Electrochem.*, vol. 43, no. 5, pp. 533–540, May 2013.

[9] K. Y. Lee, W. S. Ryu, S. I. Cho, and K. H. Lim, "Comparative study on power generation of dual-cathode microbial fuel cell according to polarization methods," *Water Res.*, vol. 84, pp. 43–48, Nov. 2015.

[10] V. J. Watson and B. E. Logan, "Analysis of polarization methods for elimination of power overshoot in microbial fuel cells," *Electrochem. Commun.*, vol. 13, no. 1, pp. 54–56, Jan. 2011.

[11] *MultiEmStat–4, 8 or 12 Channel Potentiostat*, PalmSens, Dordrecht, The Netherlands, 2016.

[12] *Electrochemistry Instruments*, Biologic, France, U.K., 2016.

[13] A. A. Rowe et al., "Cheapstat: An open-source, 'do-it-yourself' potentiostat for analytical and educational applications," *PLoS ONE*, vol. 6, no. 9, Sep. 2011, Art. no. e23783.

[14] E. S. Friedman, M. A. Rosenbaum, A. W. Lee, D. A. Lipson, B. R. Land, and L. T. Angenent, "A cost-effective and field-ready potentiostat that poises subsurface electrodes to monitor bacterial respiration," *Biosensors Bioelectron.*, vol. 32, no. 1, pp. 309–313, Feb. 2012.

[15] M. D. M. Dryden and A. R. Wheeler, "Dstat: A versatile, open-source potentiostat for electroanalysis and integration," *PLoS ONE*, vol. 10, no. 10, Oct. 2015, Art. no. e0140349.

[16] M. M. Ahmadi and G. A. Jullien, "Current-mirror-based potentiostats for three-electrode amperometric electrochemical sensors," *IEEE Trans. Circuits Syst. I, Reg. Papers*, vol. 56, no. 7, pp. 1339–1348, Jul. 2009.

[17] S. Hwang and S. Sonkusale, "CMOS VLSI potentiostat for portable environmental sensing applications," *IEEE Sensors J.*, vol. 10, no. 4, pp. 820–821, Apr. 2010.

[18] S. Ghanbari, M. Habibi, and S. Magierowski, "A high-efficiency discrete current mode output stage potentiostat instrumentation for self-powered electrochemical devices," *IEEE Trans. Instrum. Meas.*, vol. 67, no. 9, pp. 2247–2255, Sep. 2018.

[19] L. Boquete *et al.*, "A portable wireless biometric multi-channel system," *Measurement*, vol. 45, no. 6, pp. 1587–1598, Jul. 2012.

[20] G. C. Zafeiropoulos, K. I. Papadimitriou, and E. M. Drakakis, "Performance ANd ACcuracy in Electrical BioActivity recordings (PANACEA): A high-performance, wireless, multi-instrument for potentiometric and amperometric recording of biosignals," *Measurement*, vol. 129, pp. 128–141, Dec. 2018.

[21] M. Vergani *et al.*, "Multichannel bipotentiostat integrated with a microfluidic platform for electrochemical real-time monitoring of cell cultures," *IEEE Trans. Biomed. Circuits Syst.*, vol. 6, no. 5, pp. 498–507, Oct. 2012.

[22] I. Ramfos, S. Blionas, and A. Birbas, "Architecture of a modular, multichannel readout system for dense electrochemical biosensor microarrays," *Meas. Sci. Technol.*, vol. 26, no. 1, Nov. 2015, Art. no. 015701.

[23] Y. Hu, S. Sharma, J. Weatherwax, A. Cass, and P. Georgiou, "A portable multi-channel potentiostat for real-time amperometric measurement of multi-electrode sensor arrays," in *Proc. IEEE Int. Symp. Circuits Syst. (ISCAS)*, May 2016, pp. 1306–1309.

[24] A. J. Bard and L. R. Faulkner, *Electrochemical Methods: Fundamentals and Applications*, 2nd ed. Hoboken, NJ, USA: Wiley, 2000.

[25] Z. Lu *et al.*, "Biological capacitance studies of anodes in microbial fuel cells using electrochemical impedance spectroscopy," *Bioprocess Biosyst. Eng.*, vol. 38, no. 7, pp. 1325–1333, Jul. 2015.

[26] *Stability Analysis of Voltage-Feedback Op Amps Including Compensation Techniques*, Texas Instruments, Dallas, TX, USA, Mar. 2001.

[27] S. Bendaoud and G. Marino, "Practical techniques to avoid instability due to capacitive loading," Analog Devices, Norwood, MA, USA, Tech. Rep. 38-06, Jun. 2004.

[28] K. Blake, "Driving capacitive loads with Op amps," Microchip Technol., Chandler, Arizona, USA, Tech. Rep. AN884, 2003.

[29] *Operational Amplifier Stability Compensation Methods for Capacitive Loading Applied to TS507*, STMicroelectronics, Geneva, Switzerland, Nov. 2007.

[30] S. M. R. Hasan, "Stability analysis and novel compensation of a CMOS current-feedback potentiostat circuit for electrochemical sensors," *IEEE Sensors J.*, vol. 7, no. 5, pp. 814–824, May 2007.

[31] P. Weßkamp, P. Haußmann, and J. Melbert, "600-A test system for aging analysis of automotive li-ion cells with high resolution and wide bandwidth," *IEEE Trans. Instrum. Meas.*, vol. 65, no. 7, pp. 1651–1660, Jul. 2016.

[32] R. Pinto, B. Tartakovsky, and B. Srinivasan, "Optimizing energy productivity of microbial electrochemical cells," *J. Process Control*, vol. 22, no. 6, pp. 1079–1086, Jun. 2012.

[33] T. R. Molderez, B. de Wit, K. Rabaey, and M. Verhelst, "Successive parabolic interpolation as extremum seeking control for microbial fuel & electrolysis cells," in *Proc. 43rd Annu. Conf. IEEE Ind. Electron. Soc. (IECON)*, Oct./Nov. 2017, pp. 3128–3133.

[34] *A Comprehensive Study Howland Current Pump*, document 75265, Texas Instruments, Dallas, TX, USA, 2013.

[35] T. R. Molderez, X. Zhang, M. Verhelst, and K. Rabaey, "An integrated sensor board for real-time optimization of the electrical settings of a microbial electrolysis cell," in *Proc. Int. Conf. Bio-Sens. Technol.*, vol. 5, Riva Del Garda, Italy, May 2017, pp. 3128–3133.

[36] K. Guo *et al.*, "Effects of surface charge and hydrophobicity on anodic biofilm formation, community composition, and current generation in bioelectrochemical systems," *Environ. Sci. Technol.*, vol. 47, no. 13, pp. 7563–7570, Jun. 2013.

[37] T. Ramsden, M. Ruth, V. Diakov, M. Laffen, and T. A. Timbario, "Hydrogen pathways," Nat. Renew. Energy Lab., Golden, CO, USA, Tech. Rep. NREL/TP-6A10-60528, Mar. 2013.

[38] J.-Y. Nam and B. E. Logan, "Optimization of catholyte concentration and anolyte phs in two chamber microbial electrolysis cells," *Int. J. Hydrogen Energy*, vol. 37, no. 24, pp. 18622–18628, Dec. 2012.

[39] Y.-Z. Wang, L. Zhang, T. Xu, and K. Ding, "Influence of initial anolyte pH and temperature on hydrogen production through simultaneous saccharification and fermentation of lignocellulose in microbial electrolysis cell," *Int. J. Hydrogen Energy*, vol. 42, no. 36, pp. 22663–22670, Sep. 2017.

Tom R. Molderez was born in Genk, Belgium, in 1992. He received the B.S. and M.S. degrees in electrical engineering from KU Leuven, Leuven, Belgium, in 2013 and 2015, respectively. He studied his first master year at the KTH Royal institute of Technology, Stockholm, Sweden, in an Erasmus agreement. He is currently pursuing the Ph.D. degree in intelligent, parallel, low-cost measurement, and stimulation electronics to study microbial electrochemical reactors.

In 2015, he joined the ESAT-MICAS Laboratories, KU Leuven, as a Research Assistant funded through an individual grant from Research Foundation–Flanders (FWO).
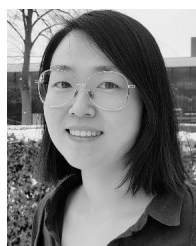
Xu Zhang received the B.S. degree in environmental science and the M.S. degree in environmental engineering from the Harbin Institute of Technology, Harbin, China, in 2012 and 2014, respectively. She is currently pursuing the Ph.D. degree with the Center for Microbial Ecology and Technology, Ghent University, Ghent, Belgium.

She was a visiting student with ITOB, Universidade Nova de Lisboa, Lisbon, Portugal, in 2016. She is currently involved in enhancement induced by periodic polarization on anodic electroactive biofilms. Her current research interests include the further understanding and future improvements of electroactivity of anodic biofilms grown under periodic polarization.

Korneel Rabaey received the Ph.D. degree from Ghent University, Ghent, Belgium, in 2005.

He is currently a Professor with the Center for Microbial Ecology and Technology, Department of Biochemical and Microbial Technology, Ghent University, and an Honorary Professor with The University of Queensland, Brisbane, QLD, Australia. He has authored or co-authored over 170 refereed articles attracting over 21 000 citations in the past ten years, listing him as an ISI Highly Cited Researcher. His current research interests include resource recovery from wastewater, decentralized treatments, industrial liquid sidestreams, and CO_2 streams from industry. Typically a combination of electrochemical and/or microbial approaches is used to achieve formation of added value products.

Prof. Rabaey is a member of the Young Academy, a fellow of the International Water Association, and one of the founders of CAPTURE. He is currently leading several scale-up projects related to organics recovery, fermentation, CO_2 conversion to organics, and sanitation in Indian slums. He was a Laureate of the Royal Academy (Belgium) in 2016. He is currently an Associate Editor of *mSystems* and an Editorial Advisory Board Member for Environmental Science and Technology.

Marian Verhelst received the Ph.D. degree from KU Leuven, Leuven, Belgium, in 2008.

In 2005, she joined BWRC of UC Berkeley, Berkeley, CA, USA, as a Visiting Scholar. She was a Research Scientist at Intel Labs, Hillsboro, OR, USA, from 2008 to 2011. She is currently an Associate Professor with the MICAS Laboratories, EE Department, KU Leuven. Her current research interests include embedded machine learning, hardware accelerators, self-adaptive circuits and systems, and low-power sensing and processing for the Internet of Things.

Prof. Verhelst is a member of the DATE Conference Executive Committee and was a member of the TPCs of DATE, ESSCIRC, and ISSCC and of the ISSCC Executive Committee. She is an Associate Editor for IEEE TVLSI and was a TCAS-II and JSSC AE and SSCS Distinguished Lecturer. She currently holds a prestigious ERC Starting Grant from the European Union.